Paleoceanography and Paleoclimatology

RESEARCH ARTICLE
10.1029/2019PA003574

Paleoproductivity in the SW Pacific Ocean During the Early Holocene Climatic Optimum

H. C. Bostock[1], J. G. Prebble[2], G. Cortese[2], B. Hayward[3], E. Calvo[4], L. Quirós-Collazos[4], M. Kienast[5], and K. Kim[6]

[1]National Institute of Water and Atmospheric Research, Wellington, New Zealand, [2]GNS Science, Lower Hutt, New Zealand, [3]Geomarine Research, Auckland, New Zealand, [4]Institute of Marine Sciences, Barcelona, Spain, [5]Department of Oceanography, Dalhousie University, Halifax, Nova Scotia, Canada, [6]Korea Polar Research Institute, Incheon, South Korea

Key Points:
- There is evidence for a small increase in productivity in subtropical water and an expanded subtropical frontal region during the early Holocene
- The expansion of the Subtropical Front is likely due to changes in the Southern Hemisphere Westerly Wind split-jet structure
- The early Holocene is not a suitable analog for future productivity for the end of the century Representative Concentration Pathway 8.5

Supporting Information:
- Supporting Information S1
- Table S1

Correspondence to:
H. C. Bostock,
helen.bostock@niwa.co.nz

Citation:
Bostock, H. C., Prebble, J. G., Cortese, G., Hayward, B., Calvo, E., Quirós-Collazos, L., et al. (2019). Paleoproductivity in the SW Pacific Ocean during the early Holocene climatic optimum. *Paleoceanography and Paleoclimatology*, *34*, 580–599. https://doi.org/10.1029/2019PA003574

Received 28 JAN 2019
Accepted 27 MAR 2019
Accepted article online 31 MAR 2019
Published online 17 APR 2019

©2019. American Geophysical Union. All Rights Reserved.

Abstract The oceans are warming, but it is unclear how marine productivity will be affected under future climate change. In this study we examined a wide range of paleoproductivity proxies along a latitudinal transect (36–58°S) in the SW Pacific during the early Holocene climatic optimum, to explore regional patterns of productivity in a slightly warmer-than-present world. During the early Holocene there is a small increase in productivity in the subtropical waters, no change at the subtropical frontal zone, and conflicting evidence in records immediately south of the subtropical front, where an increase is inferred from one core site, but not at the other. Evidence for an increase in productivity in Antarctic Surface Waters, south of the polar front, is also equivocal. We infer a small increase in productivity in subtropical waters, and the ocean just south of the subtropical front was associated with changes in the ocean circulation of the SW Pacific, driven by changes in the Southern Hemisphere Westerly Winds split-jet structure in this region. The relatively modest warming during the early Holocene climatic optimum in the SW Pacific indicates that this time period may provide an analog for future productivity for the midcentury (2055) under Intergovernmental Panel on Climate Change Representative Concentration Pathway 8.5 or for the end of the century (2100) under Representative Concentration Pathway 4.5. However, higher-resolution, downscaled models, with realistic Southern Hemisphere Westerly Winds, will be necessary to forecast future productivity for this oceanographically complex region.

1. Introduction

There is unambiguous evidence over the past few decades of increasing global temperatures as a result of anthropogenic climate change. However, it is less clear what the impact of this temperature change, and other associated changes in the global climate and oceans such as changes in stratification, density, circulation, and chemistry, will have on biological ecosystems and biogeochemistry of the oceans. A recent assessment of the outputs from the Earth system models (ESMs) included in Coupled Model Intercomparison Project (CMIP5) for the New Zealand region for the current and future climate (following Representative Concentration Pathway [RCP] 8.5) suggests that by 2055 the sea surface temperatures (SSTs) in the southwest Pacific will be an average 1 °C warmer and by 2100 AD the SSTs will have increased by an average of 2.5 °C (Law et al., 2017; Rickard et al., 2016). The CMIP5 models suggest that under RCP8.5, the predicted SSTs warming by the end of century will be accompanied by increased stratification of the upper ocean and a decrease in surface nutrients, chlorophyll *a*, and integrated net primary productivity in subtropical waters (STW) around New Zealand (Law et al., 2017; Rickard et al., 2016). In the cool subantarctic waters (SAW) the ESM ensemble for RCP8.5 end of century suggests no significant change in surface nutrients, chlorophyll *a*, or integrated primary productivity (based on the magnitude of the multimodel mean change being greater than the intermodal standard deviation (sd) and more than 80% of the models agreeing on the sign of the mean change; Rickard et al., 2016).

Another approach to understand possible changes to ocean productivity as the ocean warms is to explore changes in paleoproductivity associated with increases in ocean SSTs in the geological past. Here we examine a range of paleoproductivity proxies along a latitudinal transect (36–58°S) in the SW Pacific during the early Holocene climatic optimum (between 12 and 9 ka), when SSTs in the middle Southern Hemisphere latitudes (30–60°S) were up to 1 °C warmer than preindustrial (Marcott et al., 2013). This work is an extension of a recent study looking at SST proxies across the early to middle Holocene from the same latitudinal

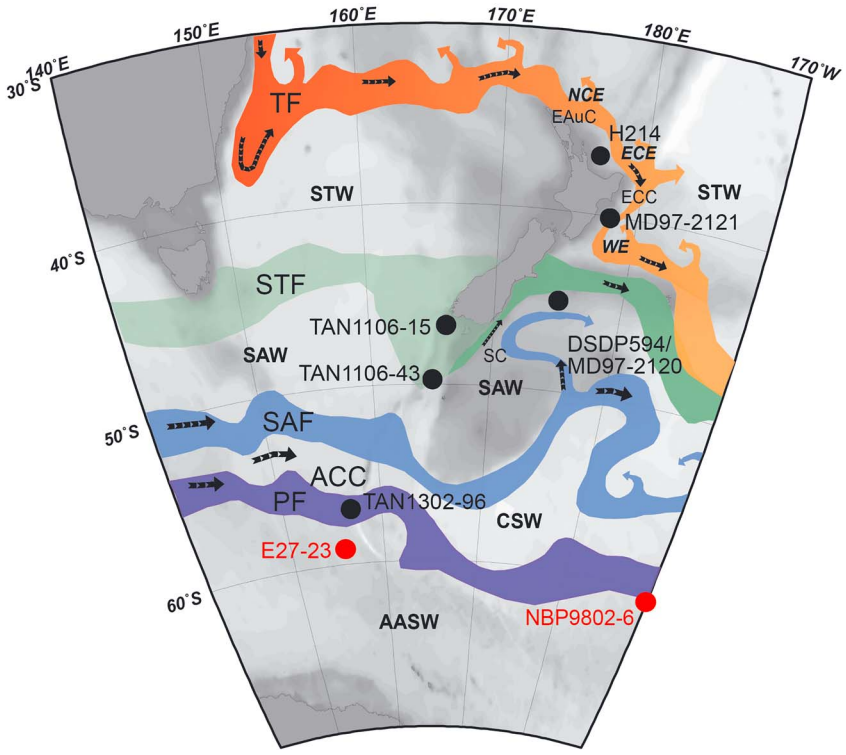

Figure 1. Map of the oceanography of the New Zealand region (adapted from Chiswell et al., 2015), showing the location of the cores used in this study (in black) and cores referred to (in red). STW = subtropical waters; SAW = subantarctic waters; CSW = Circumpolar Surface Waters; AASW = Antarctic Surface Waters; TF = Tasman Front; STF = Subtropical Front; SAF = Subantarctic Front; PF = Polar Front; EAuC = East Auckland Current; ECC = East Cape Current; ACC = Antarctic Circumpolar Current; ECE = East Cape Eddy; NCE = North Cape Eddy; WE = Wairarapa Eddy.

transect of high-resolution sediment cores straddling all the major fronts and water masses east and south of New Zealand (Prebble et al., 2017; Figure 1).

Most previous studies of marine paleoproductivity in the SW Pacific have focused on the glacial to interglacial changes and have used a wide range of different proxies (Nelson et al., 1993; Kowalski & Meyers, 1997; Carter et al., 2000; Chase et al., 2003; Calvo et al., 2004; Sachs & Anderson, 2005; Anderson et al., 2009; Bradtmiller et al., 2009; Durand et al., 2017). While, on glacial/interglacial timescales, biological productivity in the oceans has a major role in regulating the atmospheric CO_2 concentrations and thus global climate through the "biological pump" (Broecker, 1982a, 1982b), local marine biological productivity is itself affected by local conditions, including SST, oceanic circulation, macronutrient (nitrate and phosphate) and micronutrient (iron) availability, insolation, light availability, and water column mixing/stratification. Here we use a multiproxy approach to infer changes in oceanic productivity associated with SST and other environmental changes in the SW Pacific during the early to middle Holocene that may provide insight into how marine biological productivity may potentially change as the oceans warm up over the next century.

2. Regional Oceanography

2.1. Physical Oceanography

The bathymetry of the New Zealand region results in a complicated oceanographic circulation (Chiswell et al., 2015; Figure 1). Northern New Zealand is influenced by warm, oligotrophic (low nutrient) STW that originate from the East Australian Current and then flow into the New Zealand region along the Tasman Front (TF; Figure 1). When the waters in the TF reach the northern tip of New Zealand, they form the East Auckland Current (EAuC), which becomes the East Cape Current (ECC; Figure 1) as it flows east and then south along the east coast of the North Island. There are a series of semipermanent eddies associated with the EAUC and ECC, the North Cape Eddy, East Cape Eddy, and Wairarapa Eddy,

affected by the flow and the topography (Figure 1). The ECC is then diverted east along the Chatham Rise (Uddstrom & Oien, 1999), forming the northern boundary current for the Subtropical Front Zone (STFZ). A small amount of warm STW, entrained in the STFZ, also flows around the south of New Zealand and heads north along the east coast of the South Island as part of the Southland Current (SC; Sutton, 2003), before also being deflected east along the southern Chatham Rise at 44°S (Uddstrom & Oien, 1999). However, modern oceanographic measurements of the SC have found that it is predominantly made up of SAW (Sutton, 2003).

The STFZ marks the northern boundary of the Southern Ocean. It separates warm, salty, nutrient-poor STW (0–200 m depth), from fresh, cool, nutrient-rich (phosphate and nitrate) SAW to the south (Belkin & Gordon, 1996; Nodder & Northcote, 2001). The STFZ is thus characterized by steep temperature, salinity, and nutrient (nitrate and phosphate) gradients in the upper 200 m and can range from a broad transition zone in the Tasman Sea to a relatively narrow, well-constrained front east of New Zealand (Chiswell et al., 2015; Smith et al., 2013). South and east of New Zealand, the position of the Subtropical Front (STF) is strongly controlled by ocean bathymetry, being forced south around the South Island and through gaps in the Macquarie Ridge and Campbell Plateau (Smith et al., 2013) and both topographically and dynamically pinned to the southern Chatham Rise, as mentioned above (Figure 1).

Further south in the Southern Ocean, the flow is dominated by the Antarctic Circumpolar Current (ACC). The ACC is driven by strong westerly winds between 45°S and 55°S (Orsi et al., 1995). The ACC is bound to the north by the Subantarctic Front (SAF) and to the south by the Southern ACC Front, with the Polar Front (PF) positioned in between. From north to south, each of these fronts marks a distinct decline in sea surface height, SST, and salinity and an increase in nutrients, with very high nutrient concentrations (nitrate, phosphate, and silicate) south of the PF (Bostock et al., 2013). The surface waters south of the SAF are often termed *Circumpolar Surface Waters*, while the waters south of the PF are defined as Antarctic Surface Waters (AASW). As the ACC extends through the full water column, the fronts associated with the ACC are deflected by the bathymetry as they circumscribe the Southern Ocean (Sokolov & Rintoul, 2009), and south of New Zealand, the SAF and PF are forced through gaps in the Macquarie Ridge (Sokolov et al., 2006) and south and east around the Campbell Plateau (Neil et al., 2004; Figure 1).

2.2. Biological Productivity

Primary productivity in the modern southwest Pacific is highly variable spatially and temporally. A recent assessment of 13 years of Sea-viewing Wide Field-of-view Sensor (Sea-WiFS) data for this region found the most dominant feature to be the broad band of high chlorophyll *a* extending east of Southern Australia and around the south of New Zealand, continuing east along the Chatham Rise (Chiswell et al., 2013). This band of high-mean-surface chlorophyll *a* is associated with the STFZ, where the warm, macronutrient-poor, iron-rich STW meet with the cool, macronutrient-rich, micronutrient (iron)-poor SAW (Boyd et al., 1999; Nodder et al., 2005). The STFZ waters, especially those over the Chatham Rise, have the highest-mean-annual chlorophyll *a* concentrations in the region (1 mg Chl a/m^3), and this region is very important for New Zealand's commercial fisheries. High chlorophyll *a* values are also found associated with eddy activity and the continental shelf, especially around the subantarctic islands on the Campbell Plateau (Chiswell et al., 2013; Murphy et al., 2001). The reason for the high productivity around the shallow topography of the continental shelf and islands is thought to be due to a source of iron from either the terrigenous sediments or mixing in the water column (Graham et al., 2015; Murphy et al., 2001), which is the main nutrient-limiting biological productivity in the high-nutrient, low-chlorophyll (HNLC) waters of the Southern Ocean (Boyd et al., 1999, 2000, 2004; Ellwood et al., 2008).

The annual cycle in chlorophyll *a* from satellite data shows an autumn-winter-spring bloom in the STW and STFZ waters and a summer bloom in SAW (Chiswell et al., 2013). The STW/STFZ bloom is associated with an increased mixed layer depth related to increased wind stress events during these seasons, while the summer bloom in the SAW shows no correlation to wind (Chiswell et al., 2013).

North of the STFZ, the chlorophyll *a* blooms are associated with increases in the flux of biosiliceous, carbonate, and organic carbon-rich material to sediment traps in the deep ocean (Nodder et al., 2016). There is also a large flux of biomarkers (alkenones—produced by coccolithophores—and diatom sterol markers) during the spring bloom (Sikes et al., 2005). South of the STFZ in the SAW, the highest fluxes of biogenic material to

the sediment traps are also found during the spring. These are rich in biosiliceous material and are probably associated with subsurface chlorophyll *a* production, which is not observable from satellite data (Nodder et al., 2016). Alkenone flux to the SAW sediment traps make up only a small amount of the main spring bloom, peaking in late spring/early summer (Sikes et al., 2005), when the surface chlorophyll *a* concentrations are highest (Chiswell et al., 2013). The total biogenic flux to the deep ocean from SAW is 3 to 4 times less than the flux from STW, although there is considerable interannual variability in biogenic fluxes in both regions (Nodder et al., 2016).

Accompanying the increase in spring primary productivity in the STW, sediment trap time series from north of Chatham Rise display an increase in zooplankton productivity (primarily planktonic foraminiferal) during this season (King & Howard, 2001). South of Chatham Rise in the SAW, sediment trap time series also display a peak in foraminiferal export productivity in early spring, but the number of foraminifera during this peak is half that measured in the STW.

Dinoflagellate cyst assemblages have also been determined from sediment trap samples from either side of Chatham Rise (Prebble et al., 2013). These data show that there is a strong flux in dinoflagellates in spring in the STW, in agreement with an early flux of dinosterol, a biomarker of dinoflagellate production (Sikes et al., 2005), while there is a more muted seasonal variation in dinoflagellates in the SAW trap, along with a correspondingly low flux of dinosterol (Sikes et al., 2005).

3. Methods

There is no single, universally applicable paleoproductivity proxy. Therefore, this study uses a combination of biogeochemical and faunal assemblage observations that record interrelationships between surface water productivity, nutrient utilization, and efficiency of export to the deep ocean. These include carbonate mass accumulation rates (CMAR), opal mass accumulation rates (OMAR) and alkenone concentrations and mass accumulation rates (MAR), along with microfossil assemblages that provide additional information on biologically productive conditions. We also used abundances derived by micro-X-ray fluorescence (XRF) for elements that have been shown to have a potential association with productivity (Ca, Sr, Si, Ba, and Br). These productivity proxies are complemented by additional proxies to assess nutrient utilization, such as $\delta^{15}N$ of bulk sediments (which is a measure of nitrate supply versus demand), and elemental data from micro-XRF to determine the availability of potential micronutrients such as iron (Fe).

The cores were selected to form a latitudinal (36–58°S) transect from the oligotrophic STW to the HNLC conditions of the SAW and AASW (Table 1 and Figure 1; Prebble et al., 2017). The majority of the cores are currently stored in the National Institute of Water and Atmospheric Research (NIWA) core repository, except MD97-2120 and DSDP 594. Samples from DSDP 594 were requested from the International Ocean Discovery Program core repository. Following previous studies (Barrows et al., 2007; Prebble et al., 2017), we treat DSDP 594 and MD97-2120 as one core site as they are proximal to each other and have had complementary data sets analyzed on them. Samples analyzed in this study were taken close to the core top and then at a resolution of <500 years across the early to middle Holocene.

Age control for the Holocene section of the cores was provided by radiocarbon dates. These have previously been reported and calibrated by Prebble et al. (2017). Briefly, Accelerator Mass Spectrometry ages were corrected for a constant reservoir age (using the modeled reservoir age of Butzin et al., 2005, for each core location) and then calibrated using the Marine13 curve (Reimer et al., 2013) and an age model developed using the Bayesian age-depth modeling function in the R package Bchron (Haslett & Parnell, 2008). In this paper we split the Holocene following the definitions of Walker et al. (2012): the early Holocene (11.8–8.2 ka) and the mid-Holocene (8.2–4.2 ka). When comparing between the two time periods, we have used two timeslices of 2 kyr each: 11–9 ka for the early Holocene and 8–6 ka for the mid-Holocene. Linear sedimentation rates (LSR) were calculated by linear interpolation between age model tie points.

Carbonate content was measured on dried (100 °C) powdered samples using gasometric quantitative analyses after acidification (Jones & Kaiteris, 1983) with a precision of ±2%. Previously published carbonate data from DSDP 594 (Nelson et al., 1993) were included in this study. All the cores are from above the modern lysocline and carbonate compensation depth (Bostock et al., 2011); thus, dissolution of carbonate is considered minimal. Biogenic opal was measured at Dalhousie University by extraction of silica from 20-mg

Table 1
List of Cores and Proxies Analyzed on Each Core

Core	Latitude	Longitude	Water mass	Depth (m)	Temperature proxies (compiled in Prebble et al., 2017)	Productivity and nutrient proxies
H214	−36.925	177.442	STW	2,045	Foraminiferal and dinoflagellate assemblages[a]	Carbonate MAR, opal MAR, dinoflagellate index, $\delta^{15}N_{bulk}$
MD97-2121	−40.382	177.995	STW	2,314	Alkenones,[b] foraminiferal and dinoflagellate assemblages, Mg/Ca *G. bulloides*[c]2013	Carbonate MAR,[d]2006 opal MAR,[d] dinoflagellate index, alkenone concentrations,[b,e] $\delta^{15}N_{bulk}$, elemental data
TAN1106-15	−47.388	166.012	STF	2,544	Alkenones, foraminiferal and dinoflagellate assemblages	Carbonate MAR, opal MAR, dinoflagellate index, alkenone concentrations, $\delta^{15}N_{bulk}$, elemental data
DSDP 594/MD97-2120	−45.524	174.948	SAW	1,210	Alkenones,[b] foraminiferal[f] and dinoflagellate assemblages, Mg/Ca *G. bulloides*[g]	Carbonate MAR,[h] dinoflagellate index, alkenone concentrations,[i] $\delta^{15}N_{bulk}$
TAN1106-43	−50.448	164.878	SAW	3,670	Alkenones, foraminiferal and dinoflagellate assemblages	Carbonate MAR, opal MAR, dinoflagellate index, alkenone concentrations, $\delta^{15}N_{bulk}$, elemental data
TAN1302-96	−57.286	161.331	AASW	3,544	Radiolarian assemblages	Carbonate MAR, opal MAR, $\delta^{15}N_{bulk}$ elemental data

Note. STW = subtropical waters; SAW = subantarctic waters; AASW = Antarctic Surface Waters; STF = Subtropical Front; MAR = mass accumulation rates. [a]Samson et al. (2005). [b]Pahnke and Sachs (2006). [c]Marr et al. (2013). [d]Carter and Manighetti (2006). [e]Unpublished data provided by Katharina Pahnke. [f]Wells and Okada (1997). [g]Nelson et al. (1993). [h]Pahnke et al. (2003). [i]Sachs & Anderson (2005).

subsamples by a 2-M Na_2CO_3 solution at 85 °C for 5 hr. Dissolved silica concentrations in the extract were determined by molybdenum blue spectrophotometry (Mortlock & Froelich, 1989). Percent opal is calculated as 2.4 × silica. The relative standard error from duplicates was ±2.1%. Previously published low-resolution opal data from core MD97-2121 (Carter & Manighetti, 2006) were also included and were determined by X-ray diffraction following a 24-hr, 1000 °C heat conversion of opal to cristobalite (Ellis & Moore, 1973).

CMAR and OMAR were determined using the following equation:

$$\mathrm{MAR}\left(\mathrm{g{\cdot}cm^{-2}{\cdot}kyr^{-1}}\right) = \mathrm{LSR}{\times}\mathrm{DBD}{\times}\mathrm{CaCO_3}\%\text{or Opal}\%$$

Dry bulk density (DBD) was only directly measured on core MD97-2121 (Carter & Manighetti, 2006). DBD was estimated for the other core sites using the equation developed by Carter et al. (2000) for cores from the New Zealand region:

$$\mathrm{DBD}\left(\mathrm{g/cm^3}\right) = 0.85{-}0.0033X + 4.23\exp^{-5}X^2$$

where X is the % carbonate.

Alkenone analyses were performed at the Marine Science Institute in Barcelona (ICM-CSIC) following procedures detailed in Calvo et al. (2003). The concentration of long-chain alkenones, in particular diunsaturated and triunsaturated C37 alkenones, are used here to trace the input of Haptophyta algae, such as the coccolithophore *Emiliania huxleyi*, the most abundant source of alkenones in today's open ocean. The reproducibility of the analytical methodology was tested with a homogenous sediment standard, which gave analytical relative errors of ±4%.

Foraminiferal counts are those presented in Prebble et al. (2017). Based on planktonic foraminiferal assemblage counts from 891 core tops from around the Southern Hemisphere oceans, Crundwell et al. (2008) categorized *Globigerina bulloides*, *Globigerinita glutinata*, and *Globigerina quinqueloba* as the main eutrophic species that dominate sea floor assemblages in regions of high sea surface productivity. Here we have used a foraminiferal (eutrophic) productivity index = % *G. bulloides* + % *G. glutinata* + % *G. quinqueloba*. However, these species also respond to SST, with *G. bulloides* being primarily a temperate species, while *G. glutinata* being more subtropical (Crundwell et al., 2008).

Dinoflagellate cyst census counts were made on samples processed using standard methods and were previously published in Prebble et al. (2017). Assessment of the dinoflagellate cyst assemblages from 311

Southern Hemisphere core tops shows that most of the variance in the assemblages can be explained by SST but that there is also some sensitivity to productivity, coastal proximity, and bottom water oxygen (Prebble et al., 2013). We infer relative primary productivity by plotting the ratio of two groups of taxa. Group 1 includes *Selenopemphix quanta*, *S. nephroides*, *Brigantedinium* spp., *Trinovantedinium applanatum, Echinidinium* spp., *Spiniferites membranaceus*, and *S. mirabilis*, which are generally found in samples from shallow waters near to shore and/or beneath areas of relatively high surface primary productivity. Group 2 includes *Impagidinium aculeatum*, *I. paradoxum*, *I. patulum*, *I. variaseptum*, *I. pallidum*, *Dalella chathamense*, and *Pyxidinopsis reticulata*, which are more abundant in samples distal from shore in more oligotrophic settings. This dinoflagellate cyst productivity index is the ratio of Group 1/Group 2, the ratio of selected peridinioid cysts to oceanic gonyaulaucoid cysts. It should be noted that peridinioid cysts are more susceptible to oxidation in seafloor depositional settings with low oxygen than are gonyaulaucoid cysts (Zonneveld et al., 1997, 2008, 2010): Variations in sea floor oxygenation levels could therefore bias the downcore preservation of the cysts and thus the productivity index values.

Micro-XRF scanning was undertaken on several of the cores (except H214 and DSDP 594/MD97-2120, which have insufficient sediment remaining). U-channels (2 cm × 1 cm × 30 cm) were subsampled from the archive half of the cores. The U-channels were continuously analyzed for chemical elements using an Itrax™ XRF scanner at 2-mm resolution at the Korean Polar Research Institute. The productivity elements (Ca, Sr, Si, Ba, and Br) were normalized with elements that represent terrigenous flux (e.g., Ti or Fe). The use of ratios is recommended for this kind of data as it avoids closed sum effects (Rothwell & Croudace, 2015).

Nitrogen isotopes are a measure of the nitrate "utilization" (supply versus demand; Altabet & Francois, 1994). Phytoplankton in the ocean preferentially incorporate the lighter isotope of N, ^{14}N; thus, when nitrate is present in excess, organic matter will have a lower $^{15}N/^{14}N$ ratio (denoted $\delta^{15}N$). In addition to biological productivity, the $\delta^{15}N$ can also be altered by N-fixation (which lowers $\delta^{15}N$) or denitrification (which raises $\delta^{15}N$). There may be rare occurrences of N-fixation in the STW (following a cyclone; Law et al., 2011), but there is no evidence for denitrification in the modern ocean waters around New Zealand. Assuming that neither of these processes was important in this region during the Holocene, and that sedimentation rates are sufficient to minimize diagenetic alteration (Robinson et al., 2012), then the $\delta^{15}N$ of the organic matter in sediments represents changes in either the productivity or the nutrient supply. Given the paucity of sedimentary $\delta^{15}N_{bulk}$ records from the region at large (Galbraith et al., 2013), we cannot rule out that the $\delta^{15}N_{bulk}$ records and thus our interpretations are aliased to some degree by upstream changes in the isotopic composition of the nitrate itself. Nitrogen isotope ratios were determined at Dalhousie University on freeze-dried, ground bulk samples using a Fisons NA1500 element analyzer coupled to a VG prism mass spectrometer in a continuous flow of helium. The $\delta^{15}N$ values are reported relative to air N_2 with an analytical precision of ±0.2‰ (Kienast et al., 2005).

4. Results

The results of the downcore proxy data are shown in Figures 2–4 and summarized below. The averages for the early Holocene timeslice (11–9 ka), mid-Holocene timeslice (8–6 ka), and late Holocene (0–2 ka) are provided in Figure 5 (and supporting information Table S2).

The highest carbonate contents ($CaCO_3$%) are found in core TAN1106-43 (Figure 2a), which is more distal from the New Zealand landmass, other than core TAN1302-96 (Figure 1). However, TAN1106-43 has relatively low CMAR (Figure 2b) due to the lower LSR in this core (Figure 2e). The highest CMAR are present in cores MD97-2121 and TAN1106-15 with values between 2 and 7 $g{\cdot}cm^{-2}{\cdot}kyr^{-1}$ (Figure 2b), with an average of ~3 $g{\cdot}cm^{-2}{\cdot}kyr^{-1}$ during the Holocene, also reflected in the very high LSR in these cores (Figure 2e). MD97-2121 shows slightly higher CMAR in the early Holocene (Figure 5), but due to the high variability of the CMAR, it is within error of the rest of the Holocene. DSDP 594/MD97-2120 also displays high CMAR in the early Holocene and is the only core that has significantly higher (greater than the sd of the variability) CMAR in the early Holocene timeslice (than in the mid-Holocene; Figures 2b and 5 and Table S2).

The percent of biogenic opal is low in all of the cores (<10%) except the AASW core, TAN1302-96 (55–80%; Figure 2c). In general, the OMAR are very low for the northern cores, with only MD97-2121 showing values higher than 1 $g{\cdot}cm^{-2}{\cdot}kyr^{-1}$, ranging from 2.7 to 0.8 $g{\cdot}cm^{-2}{\cdot}kyr^{-1}$ (Figure 2d). Core

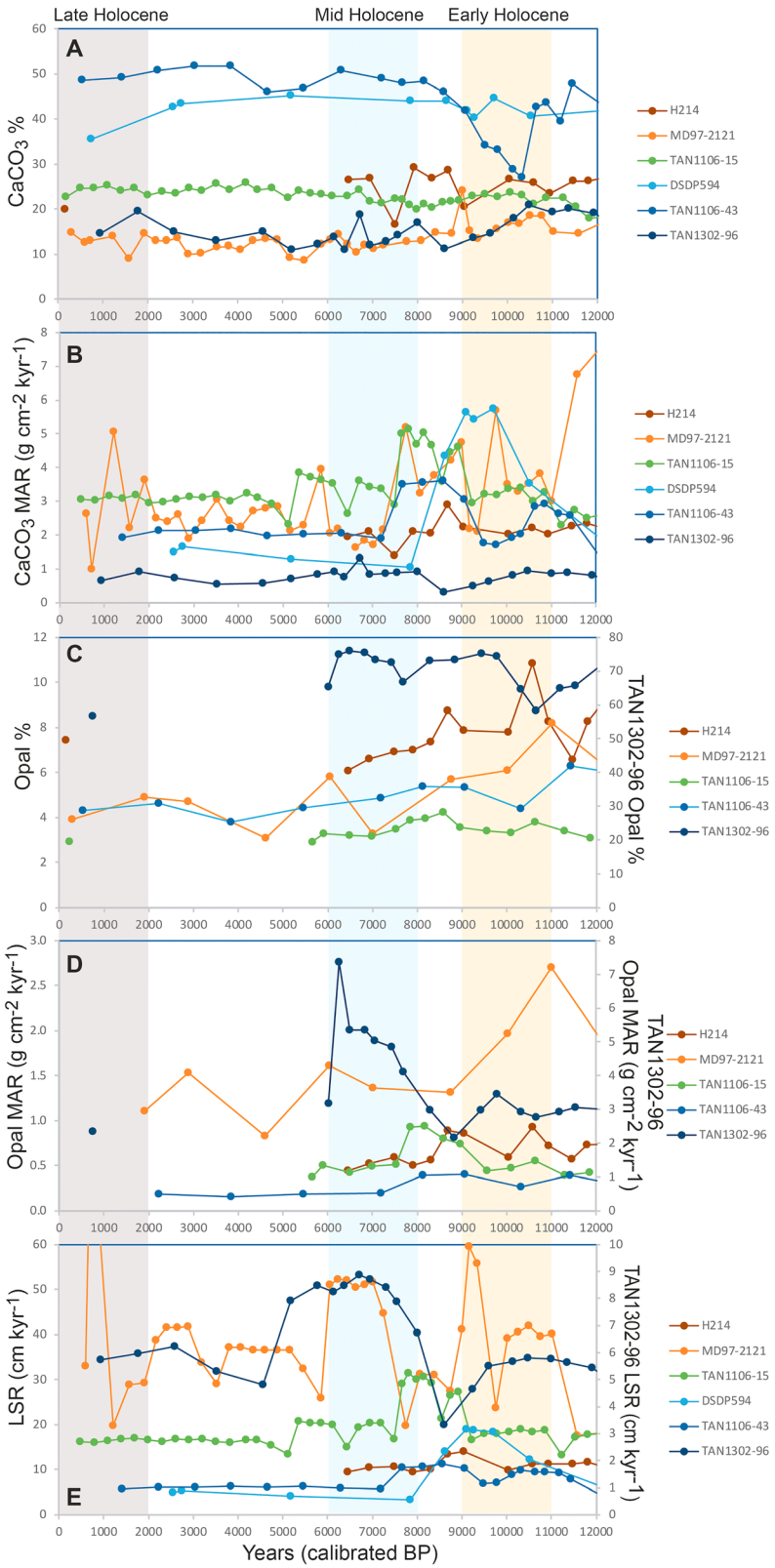

Figure 2. (a) $CaCO_3$%, (b) carbonate mass accumulation rates (MAR), (c) opal%, (d) opal MAR, (e) linear sedimentation rates (LSR). Alternative *y*-axis on all the graphs is for core TAN1302-96. The orange shaded bar is the early Holocene timeslice (11–9 ka), the blue shaded bar is the mid-Holocene timeslice (8–6 ka), and the light gray shaded bar is the late Holocene (2–0 ka). The averages for the shaded timeslices can be found in the supporting information and Figure 5.

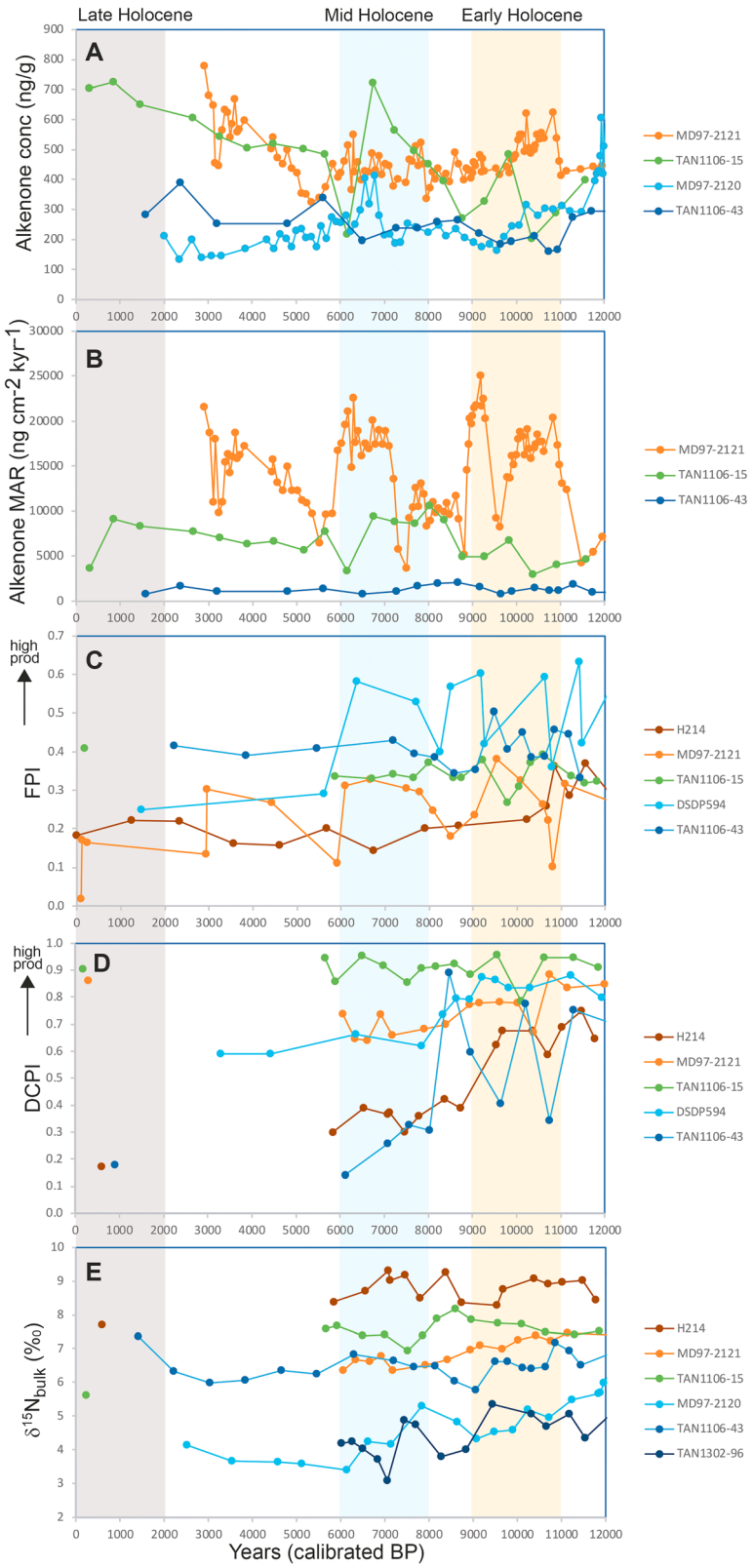

Figure 3. (a) Alkenone concentrations, (b) alkenone mass accumulation rates (MAR), (c) foraminiferal productivity index (FPI), (d) dinoflagellate cyst productivity index (DCPI), and (e) $\delta^{15}N_{bulk}$. The orange shaded bar is the early Holocene timeslice (11–9 ka), the blue shaded bar is the mid-Holocene timeslice (8–6 ka), and the light gray shaded bar is the late Holocene (2–0 ka). The averages for the shaded timeslices can be found in the supporting information and Figure 5.

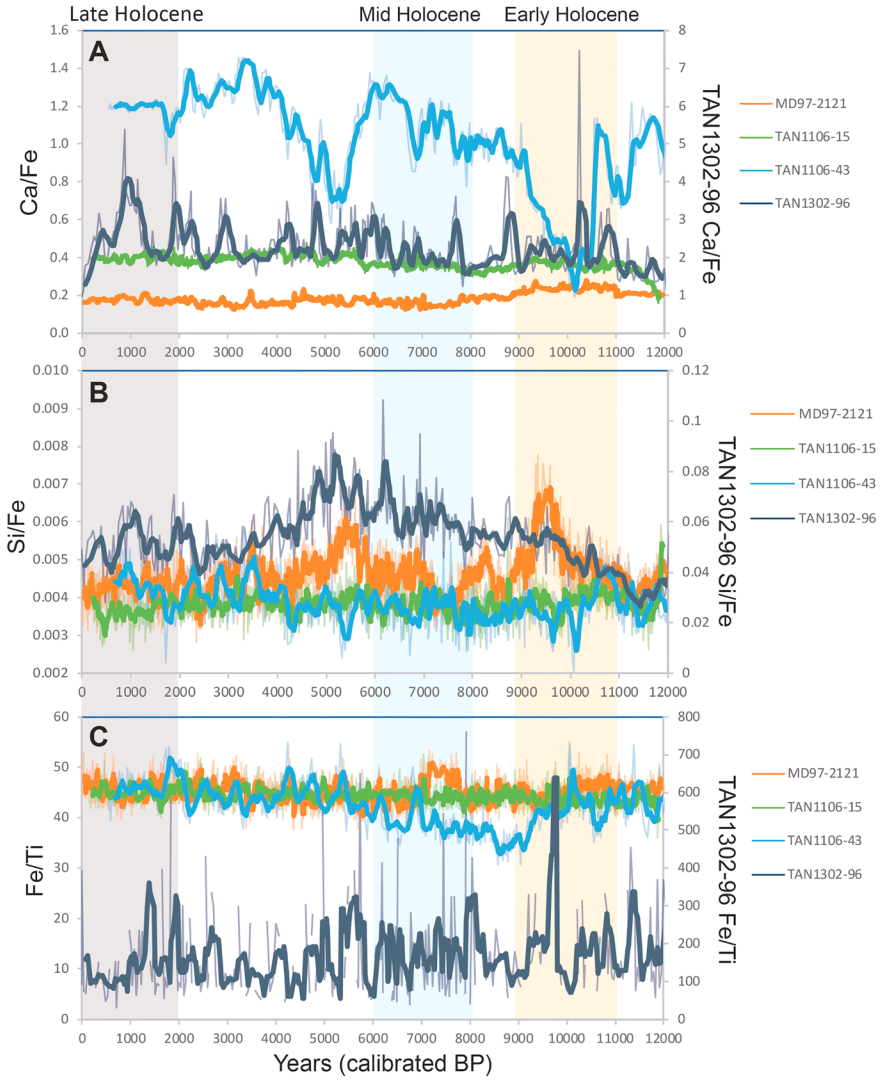

Figure 4. (a) Ca/Fe, (b) Si/Fe, and (c) Fe/Ti ratios from the micro-X-ray fluorescence. Alternative *y*-axis on all the graphs is for core TAN1302-96. A 5-point running mean is shown in the bold lines for each of the cores, while the raw data are displayed in the background. The orange shaded bar is the early Holocene timeslice (11–9 ka), the blue shaded bar is the mid-Holocene timeslice (8–6 ka), and the light gray shaded bar is the late Holocene (2–0 ka). The averages for the shaded timeslices can be found in supporting information and Figure 5.

MD97-2121 displays slightly elevated (above sd) OMAR during the early Holocene than during the middle or late Holocene, while TAN1302-96 displays significantly higher OMAR during the mid-Holocene timeslice (Table S2 and Figures 2d and 5).

The highest alkenone concentrations are found in cores MD97-2121 (Pahnke and Sachs, personal communication, February 2015) and TAN1106-15 (Figure 3a). However, neither of these cores show elevated alkenone concentrations during the early Holocene than during the rest of the Holocene (within sd; Figures 3a and 5). In core MD97-2120 the alkenone concentrations peak just prior to the early Holocene with values of 400–600 ng/g (Figure 3a; Sachs & Anderson, 2005) but then drop down to values of 200–300 ng/g during the Holocene (Figure 3a). These general patterns remain when alkenone MAR for MD97-2121, TAN1106-15, and TAN1106-43 are considered (Figure 3b). MD97-2121 has the highest alkenone MAR, and TAN1106-43 the lowest, primarily reflecting the sedimentation rates in the core (Figure 2e). Alkenone MAR cannot be calculated for MD97-2120 due to the fact that the DBD has not been determined for this core (only for the DSDP 594 core from this site).

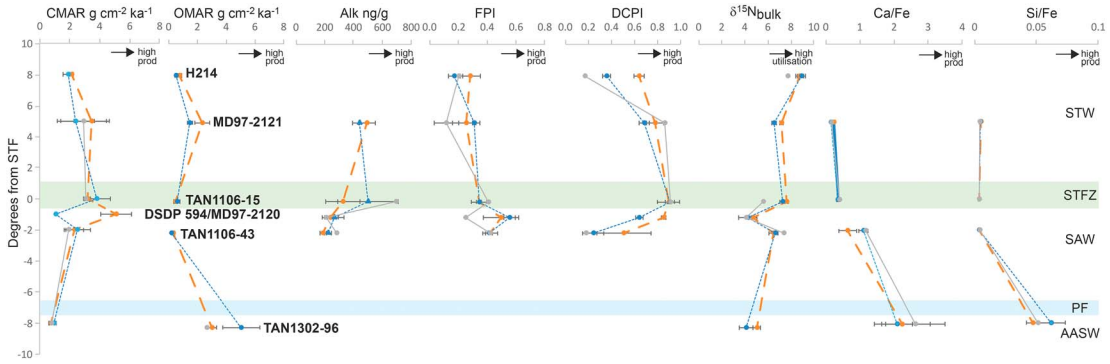

Figure 5. Latitudinal transects (displayed in terms of distance from the Subtropical Front [STF]) of the average productivity and environmental proxies (see the supporting information) in this study for the three Holocene timeslices: the early Holocene (11–9 ka; orange dashed lines), the mid-Holocene (8–6 ka; blue dotted lines), and the late Holocene (2–0 ka; gray lines). From left to right: carbonate mass accumulation rates (CMAR), opal mass accumulation rates (OMAR), alkenone concentrations, foraminiferal productivity index (FPI), dinoflagellate cyst productivity index (DCPI), $\delta^{15}N_{bulk}$, Ca/Fe, and Si/Fe. STW = subtropical waters; Subtropical Front Zone; SAW = subantarctic waters; PF = Polar Front; AASW = Antarctic Surface Waters.

The highest foraminiferal eutrophic index values are found in cores DSDP 594 and TAN1106-43, and the lowest values are found in the STW cores H214 and MD97-2121 (Figure 3c). From these results it is clear that the foraminiferal eutrophic index is anticorrelated to SST, as the index values decrease in the cores from south to north. The only core that shows a significant change through time in the foraminiferal eutrophic index is DSDP 594, with a large drop around 6 ka (Figure 3c). There is significant variability in this core driven by changes in *G. quinqueloba* (which varies from 0% to 16%) and *G. bulloides* (which varies from 50% to 30%, averaging around 40%). This variability is not related to different scientists counting the foraminiferal assemblages.

Cores TAN1106-15, MD97-2121, and DSDP 594 show the highest dinoflagellate productivity index values, while H214 and TAN1106-43 display lower values (Figure 3d). This correlates with the spatial variability of ocean productivity in the modern ocean (i.e., the highest productivity is within and adjacent to the STF). Thus, it appears that the dinoflagellate productivity index provides a more robust productivity indicator than does the foraminiferal eutrophic index. Several of the cores display significant drops in the dinoflagellate index between the early and middle Holocene. TAN1106-43 has the highest variability and shows the largest change from 0.9 to 0.3 at ~8 ka. DSDP 594 displays a large drop from 0.88 to 0.64 between 9 and 8 ka, while H214 exhibits a significant drop from 0.67 to 0.38 between 9.6 and 8.6 ka.

The $\delta^{15}N_{bulk}$ values are generally higher in the STW/STFZ (H214, MD97-2121, and TAN1106-15) and lower in the SAW (MD97-2120 and TAN1106-43) and AASW (TAN1302–96; Figure 3e). This is opposite to the surface water nitrate concentrations (Bostock et al., 2013). In general, H214, MD97-2121, and TAN1106-15 show significantly higher $\delta^{15}N_{bulk}$ values (~1‰ greater) in the early to middle Holocene than in the late Holocene (Figures 3e and 5).

The Ca/Fe ratio is highest in the TAN1302-96 as there is little terrigenous material in this core; thus, the Fe counts are much lower than in the other cores (Figure 4a). TAN1106-43 is the next highest, due to the highest $CaCO_3$%, but also the most variable. MD97-2121 is the lowest due to the high terrigenous (and volcanic ash) flux off the northeast coast of the North Island of New Zealand (Carter et al., 2000). TAN1106-15 also displays low Ca/Fe due to its close proximity to the South Island of New Zealand. Ca/Fe from these cores show no discernible patterns during the Holocene.

Si/Fe ratios range between 0.003 and 0.005 in TAN1106-15 and TAN1106-43 (Figure 4b). In MD97-2121 the background Si/Fe ratios also sit in this range; however, there are several peaks in Si/Fe at ~9.5 and ~5.5 ka, which are related to volcanic tephra deposits (Carter et al., 2008). TAN1302-96 has significantly higher Si/Fe ratios than the other cores with a range of 0.03 to 0.1 (Figure 4b), with evidence for an increase during the mid-Holocene. This higher Si/Fe ratio is interpreted to represent the high biogenic opaline silica in this core (Figure 2c).

In all the cores, Sr is highly correlated with Ca ($r > 0.75$); thus, the Sr is interpreted to primarily be incorporated in the $CaCO_3$ mineral structure and is not discussed any further. Br and Ba data are noisy and

show no correlation with other elements. The exception to this is in the TAN1302-96 core where Ba has a weak correlation with Ca ($r = 0.3$), Fe ($r = 0.48$), and Mn ($r = 0.59$). Br or Ba are not discussed further in this study.

As Fe is a redox-sensitive element and prone to diagenetic remobilization in anoxic pore waters, we also compare it with the more inert Ti to determine if there is any evidence of diagenetic alteration within the core, which would affect the Fe concentrations (Richter et al., 2006). The Fe and Ti concentrations are strongly correlated in TAN1106-43 ($r = 0.82$) and moderately correlated in MD97-2121 ($r = 0.69$) but less well correlated in cores TAN1106-15 ($r = 0.53$) and TAN1302-96 ($r = 0.18$). Fe/Ti ratios in the cores are fairly constant averaging 42–45 (TAN1106-15, TAN1106-43, and MD97-2121; Figure 4c). There are some fluctuations in Fe/Ti in MD97-2121 that are related to volcanic tephra in this core (Carter et al., 2008). Ti is very low in TAN1302-96, and therefore, the Fe/Ti ratios are significantly higher in this core. These data suggest that there is no evidence for diagenetic alteration of Fe in these cores during the Holocene. For consistency across all the cores we have chosen to ratio Ca and Si against Fe.

5. Discussion

5.1. Evidence for Productivity Changes During the Holocene

We have compiled a range of proxy data to decipher the surface water productivity, nutrient utilization, and efficiency of export to the deep ocean along the latitudinal transect east of New Zealand during the early Holocene climatic optimum. As discussed above, many of these proxies provide information on only a specific part of the ecosystem or environmental conditions, and therefore, the spatiotemporal patterns of the different proxies will not necessarily be coherent. In this section, we discuss the different productivity proxies and any evidence for increased productivity at the core sites and in the different water masses during the early Holocene than during the middle and late Holocene (summarized in Figure 5 and Table S2).

5.1.1. Subtropical Waters

The STW cores H214 and MD97-2121 display slightly higher CMAR and OMAR in the early Holocene (although only the MD97-2121 OMAR are significantly greater than sd) than in the middle or late Holocene (Figures 2b, 2d, and 5 and Table S2). There are slightly higher alkenone concentrations in MD97-2121 (Figures 3a and 5) during the early Holocene timeslice than during the mid-Holocene, but these are not significant (within sd). The dinoflagellate cyst productivity index is high in both MD97-2121 and H214 in the early Holocene, indicating higher productivity, or better preservation of the dinoflagellate Group 1 taxa, compared to that in the mid-Holocene, but MD97-2121 is higher again in the late Holocene. Nitrogen isotopes are also high in H214 ($\delta^{15}N_{bulk} > 8‰$) throughout this time period, indicating that nitrate utilization remains high throughout the Holocene. MD97-2121 $\delta^{15}N_{bulk}$ values are lower than those of H214. The $\delta^{15}N_{bulk}$ in MD97-2121 are slightly higher during the early Holocene than during the mid-Holocene (above sd; Figure 5 and Table S2), indicating high productivity or reduced supply of nitrate in the early Holocene. The Ca/Fe ratios in MD97-2121 show no major increase during the early Holocene (11–9 ka). The elevated Si/Fe in the early Holocene in this core (Figure 4b) coincide with the presence of volcanic tephra (Carter et al., 2008; Lowe et al., 2013). Thus, taking all the different productivity proxies into account, we suggest there is evidence for slightly higher biological productivity, export, and preservation in the STW during the early Holocene, than during the middle and late Holocene (Figure 5).

5.1.2. Subtropical Front Zone

The core TAN1106-15 location is under the influence of STFZ waters today, displaying high CMAR (Figure 2b; supported by the high LSR in this core; Figure 2e), high alkenone concentrations (and alkenone MAR; Figures 3a and 3b), and the highest dinoflagellate productivity index values during the late Holocene of all the cores (Figure 3c). This is also supported by relatively high $\delta^{15}N_{bulk}$ values (>7‰; Figure 3e), higher than those of MD97-2121 but less than those of H214 in STW, indicating that there is higher nitrate utilization at this location. The elemental ratios in this core show minimal variability in the Ca/Fe and Si/Fe between 12 and 6 ka (Figure 5), while the other productivity proxies (CMAR and OMAR; Figure 2; alkenone concentrations and MAR; foraminiferal eutrophic index; dinoflagellate productivity index; Figure 3) are highly variable throughout the Holocene. This suggests that there may be local factors such as currents

and winds affecting the productivity or accumulation of sediments at this core site close to the South Island of New Zealand.

5.1.3. Subantarctic Waters

Although physically north of TAN1106-15 (by latitude), core site DSDP 594/MD97-2120 sits just south of the modern STF, on the southern flank of Chatham Rise. The CMAR at DSDP 594 are 5 times greater in the early Holocene than in the middle and late Holocene (Figures 2b and 5), and dinocyst productivity index values are also higher during the early Holocene than during the middle or late Holocene (Figure 3d). Previous work has also suggested that there are slightly higher total organic carbon during the early Holocene (Kowalski & Meyers, 1997). The foraminiferal eutrophication index is highly variable in this core during the early and middle Holocene period, suggesting that the productivity was highly variable, possibly associated with alternating water masses at this site during the early to middle Holocene (Prebble et al., 2017). Thus, the majority of the productivity proxies show evidence for higher productivity at this core site during the early Holocene, than during the middle or late Holocene. The low $\delta^{15}N_{bulk}$, similar to that in the PF core TAN1302-96, thus suggests that there is a good supply of nitrate at this site during the early Holocene (Figure 3e). The decline in $\delta^{15}N_{bulk}$ during the Holocene suggests that the utilization declines with a decrease in productivity in the middle and late Holocene.

Core TAN1106-43 was retrieved just south of the modern STFZ in the Solander Trough. However, the core location is regularly influenced by the STFZ waters, as attested by the presence of warm STFZ eddies over this site when the core was collected (Smith et al., 2013). CMAR (Figure 2b) and Ca/Fe (Figure 4a) suggest that productivity was unchanged throughout the Holocene (Figure 5). The alkenone concentrations and MAR (Figures 3a and 3b), foraminiferal eutrophic index (Figure 3c), and the $\delta^{15}N_{bulk}$ (Figure 3e) also remain stable for the early and middle Holocene timeslices, with values similar to, or lower than, those of the late Holocene for these proxies. In contrast, the dinoflagellate cyst productivity index shows that productivity was slightly higher in the early Holocene (Figure 3d), but this may reflect better preservation of the Group 1 dinoflagellate cysts in the deep waters (>3,500 m) at this time (Zonneveld et al., 1997, 2008, 2010). This suggests that there is limited evidence for elevated productivity during the early Holocene at this core location, which has likely been proximal to the STFZ throughout the Holocene period (Bostock et al., 2015).

5.1.4. Antarctic Surface Waters

The AASW core TAN1302-96 displays little evidence for elevated productivity during the early Holocene. The exception is evidence for higher $\delta^{15}N_{bulk}$, which represents greater nitrate utilization, from either increased demand or a reduced supply of nitrate (Figure 3e). Given the lack of evidence for elevated productivity, the higher $\delta^{15}N_{bulk}$ may have been due to a reduction in supply from reduced upwelling at the PF during the early Holocene. Alternatively, it is conceivable that the Holocene decrease in $\delta^{15}N_{bulk}$ at this site is reflective of a decreasing $\delta^{15}N_{bulk}$ source signature, caused by decreasing nitrate consumption in the Southern Ocean HNLC region (Francois et al., 1997; Galbraith et al., 2013). Higher productivity is instead evident during the mid-Holocene, with increased (double) OMAR (resulting in a doubling of sedimentation rates; Figures 2d, 2e, and 5) and Si/Fe ratios (Figures 4b and 5). In contrast to these OMAR results of TAN1302-96, previous results from nearby cores E27-23 and NBP9802-2 (Figure 1) show that opal flux (flux calculated from ^{230}Th measurements, which takes into account horizontal transport) is slightly higher in the early Holocene than in the mid-Holocene (Anderson et al., 2009; Bradtmiller et al., 2009; Chase et al., 2003). This conflicting evidence suggests that any increase in productivity south of the PF in the early or middle Holocene may have been patchy in the SW Pacific sector of the Southern Ocean due to either local productivity variability, as seen in the modern chlorophyll *a* distribution (Bradtmiller et al., 2009), related to the exact position of the core compared to the PF, or focusing of sediment by bottom water currents. Flux measurements on TAN1302-96 will be needed to determine if the OMAR are affected by focusing of sediment at this core location.

Combining all the proxy data together, we suggest there is evidence for slightly higher productivity and preservation during the early Holocene (than during the mid-Holocene or the late Holocene) in the STW; no change in the productivity at the STFZ; and significantly higher productivity during the early Holocene at SAW core site DSDP 594/MD97-2120 just south of the STF, but not at TAN1106-43; and it is unclear if there was any change in the biological productivity in the AASW at the PF in the SW Pacific sector of the Southern Ocean at this time.

5.2. What Caused the Productivity Patterns During the Early Holocene?

Biological composition and productivity in the oceans is affected by a range of different environmental factors including SST; changes in ocean circulation and upwelling, mixing, and stratification; macronutrients (such as nitrate) and micronutrient (such as iron) concentrations; and atmospheric CO_2 concentrations. In this section, we look at the different factors that may have affected the productivity proxies during the early Holocene.

In a complementary study, a range of different SST proxies were used to assess the early Holocene SSTs using this same transect of cores (Prebble et al., 2017). In contrast to the previous global SST compilation (Marcott et al., 2013), Prebble et al. (2017) showed that the average SSTs (from a combination of multiple SST proxies) between 36°S and 58°S in the SW Pacific east of New Zealand were not statistically higher in the early Holocene than were the modern SSTs (once the calibration error ± 1 °C of the different proxies was taken into account). The exception is core site DSDP 594/MD97-2120 with an increase in SST of 2–3 °C. Prebble et al. (2017) interpreted this increase in SST at this core site as an expansion of the influence of the STFZ south of Chatham Rise. This southward expansion of STFZ influence is also the most likely explanation for the elevated productivity at DSDP 594/MD97-2120 during the early Holocene evident in this study, as the mixing of STW and SAW in the STFZ results in the highest productivity in the region today (Chiswell et al., 2013; Murphy et al., 2001).

Despite relatively stable SSTs in the other cores, there is evidence from minor changes in the SST and microfossil assemblages for small variations in early Holocene oceanic circulation of the SW Pacific that may have influenced the productivity of the region. At core site H214 slightly elevated SST (+1 °C on average; +2 °C from foraminiferal assemblages; Samson et al., 2005) in the early Holocene may have been caused by the southward shift of the TF between 12 and 11 ka (Bostock et al., 2006). Such a shift would have reinvigorated the EAuC and subtropical currents that influence the north and east of the North Island of New Zealand. This increased subtropical inflow from the TF may have led to the intensification of the semipermanent eddy features that are currently present in this region (Figure 1) and are associated with increased productivity in the modern ocean due to the upwelling of nutrients (Chiswell et al., 2013). This conceptual model may explain increased productivity in the STW during the early Holocene and is consistent with higher nitrate utilization (increased $\delta^{15}N_{bulk}$) at site H214 throughout the early and middle Holocene (Figure 6b). The most plausible interpretation of this $\delta^{15}N$ result is that productivity increased relative to supply at this time, suggesting that the increase in nutrients may have been seasonal due to winter mixing, and was then drawn down through the spring and summer. The modern satellite images show high winter and spring productivity in this region and low in summer when the nutrients have been used up (Chiswell et al., 2013; Murphy et al., 2001). Alternatively, the plankton may have been able to use nitrate more efficiently if there was a greater supply of the micronutrient Fe, which occurs in HNLC regions such as the Southern Ocean today (Franck et al., 2003). The increased Fe (and nitrate) may also be associated with the upwelling from the intensified eddies of the EAuC.

Core MD97-2121 shows slightly lower SSTs (−1 °C compared to modern) during the early Holocene (Prebble et al., 2017). This site sits at the edge of the Wairarapa Eddy today and therefore may have also been affected by increased eddy activity, resulting in both a lowered SST and an increase in productivity around the edge of the eddy (Chiswell et al., 2013). Contradicting this slightly lower SST, there is an increase in the abundance of the subtropical foraminifera *Globigerinoides ruber* in the early Holocene samples, supporting an increase in the inflow of warmer STW along the TF and around northern New Zealand (Marr et al., 2013). Foraminiferal and dinoflagellate cyst assemblages are dominated by STW assemblages in this core but also suggest that there was an increase in species associated with the STFZ in the early Holocene (Prebble et al., 2017; Scott, 2013). Thus, the higher productivity in the early Holocene at this core site may have also been due to an expansion of the STFZ to the north (Prebble et al., 2017). This influence of STFZ, or upwelling from the eddy activity, is supported by the $\delta^{15}N_{bulk}$, which are slightly lower at this core site than at the STFZ core TAN1106-15. Higher nitrate utilization (increased $\delta^{15}N_{bulk}$; Figures 3e and 5) in the early Holocene indicates that productivity was greater than supply; thus, the increase in nutrients may have been a seasonal feature (as for H214). This is supported by increased stratification of the water column during spring and summer, from oxygen isotopes of different planktonic foraminifera species (Carter et al.,

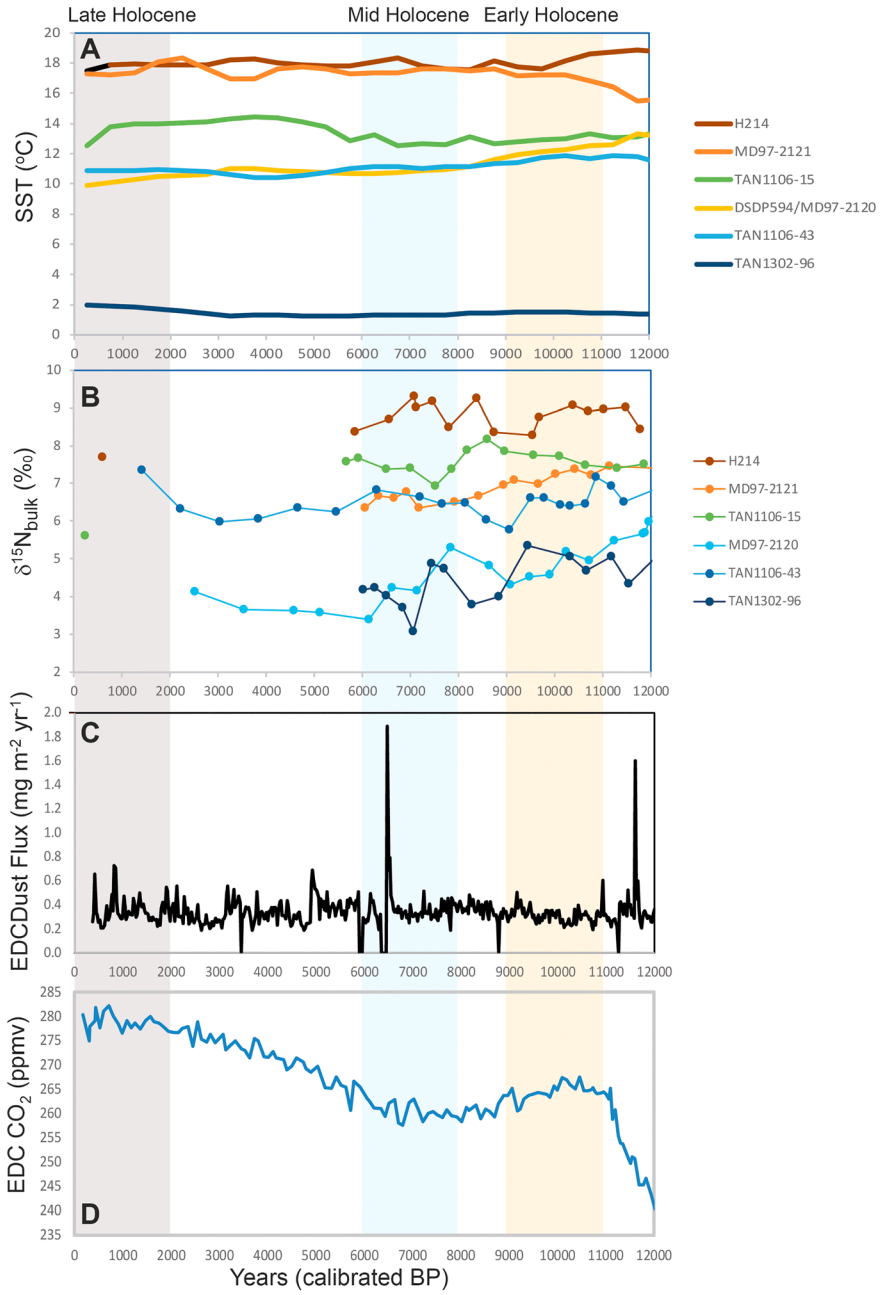

Figure 6. Environmental factors that may affect biological productivity: (a) average sea surface temperatures (SST, °C; Prebble et al., 2017); (b) $\delta^{15}N_{bulk}$ (‰; this study); (c) dust flux from European Project for Ice Coring in Antarctica (EPICA) Dome C core (on EDC3 time scale; Lambert et al., 2012); and (d) atmospheric CO_2 concentrations from EPICA (Lüthi et al., 2008). The orange shaded bar is the early Holocene timeslice (11–9 ka), the blue shaded bar is the mid-Holocene timeslice (8–6 ka), and the light gray shaded bar is the late Holocene (2–0 ka).

2008) and SST estimates from Mg/Ca on the two final test chambers of *Globigerina bulloides* that calcify at different depths (Marr et al., 2013).

The STFZ core TAN1106-15 shows slightly lower SST during the early Holocene, while TAN1106–43, which sits further south in the Solander Trough on the edge of the STFZ, exhibits slightly higher SST. It has previously been suggested that the slight increase in foraminiferal-derived SST at TAN1106-43 was due to a southward shift in the STF south of New Zealand during the early Holocene (Bostock et al., 2015). A southward shift of the influence of the STFZ is also supported by an increase in the STW foraminiferal

and dinoflagellate cyst species at TAN1106-15 and increased frequency of species associated with the STFZ at TAN1106-43, which is dominated by SAW species in the late Holocene (Prebble et al., 2017). In contrast to DSDP 594/MD97-2120, there is no obvious increase in productivity associated with this southward shift of the STFZ at these TAN1106-15 and TAN1106-43 core sites in the early Holocene (Figures 2–5). This is further supported by evidence from other productivity proxies (Org C flux, opal flux, carbonate flux, and Barium excess) from a low-resolution core in the Solander Trough (TAN0803-9; Durand et al., 2017).

The AASW core TAN1302-96 displays no evidence for an increase in SST in the early Holocene (Figure 6a; Prebble et al., 2017), and there is conflicting evidence for any increase in productivity in the AASW at this time in this core and E27-23 and NBP9802-6 (Figure 1; Chase et al., 2003; Bradtmiller et al., 2009; Anderson et al., 2009). One explanation may be that there was a small shift south in the position of the PF during the early Holocene, resulting in core TAN1302-96 being located north of the PF at that time, while cores E27-23 and NBP9802-6 remaining south of the PF. As a result, the productivity overlying cores E27-23 and NBP9802-6 remained higher as the region south of the PF has deep winter mixed layers (>60 m) in the modern ocean bringing up more nutrients (Anderson et al., 2009). This may also explain why there is a minor increase in the $\delta^{15}N_{bulk}$ in the early Holocene in TAN1302-96, as it is further from the upwelling PF and the source of nitrate. In comparison, there is no significant change in the $\delta^{15}N$ of diatoms at core site NBP9802-6, indicating that it remained within the PF (Robinson & Sigman, 2008).

Iron is an important micronutrient for plankton (Boyd et al., 1999). In MD97-2121, the Si/Fe increases at several points during the Holocene due to volcanic tephra (ash) deposition from the nearby Taupo Volcanic Zone (Carter et al., 2008; Lowe et al., 2013). While it has been suggested that Fe from volcanic tephra may lead to a transitory increase in productivity (Duggen et al., 2010), it is unlikely that this would have influenced the productivity of the entire early Holocene. Fe in STW is supplied from both below (upwelling due to winter mixing and eddy activity) and above from dust from Australia and is not considered to be a limiting micronutrient in the modern STW (Ellwood et al., 2013). Both cores MD97-2121 and TAN1106-15 show relatively stable Ca/Fe throughout the Holocene; the exception is TAN1106-43, which shows a large decrease during the early Holocene (Figure 4a). However, there is no evidence for an increase in productivity in this core at this time, and this may be due to an increase in terrigenous sediment (due to a turbidite) at this time (Bostock et al., 2015). There is evidence for a slight increase in Fe counts in TAN1302-96 (~3,300 counts for 11–9 ka versus 2,500 counts in the 8- to 6-ka time window), suggesting that Fe concentrations increased relative to other elements at this time in the Southern Ocean. This increase in Fe is surprising as there is very low dust concentrations in the Antarctic ice cores during the early Holocene (Lambert et al., 2012; Figure 6C). The increase in Fe counts may have just been relative to the other elements measured in the core at this time, as there was no increase in OMAR or Si/Fe during the early Holocene at TAN1302-96 (Figures 2c, 2d, and 4b). Thus, it does not appear that changes in Fe are influencing Holocene productivity in the SW Pacific.

Atmospheric CO_2 levels reached a peak during the early Holocene (265 ppm; Luthi et al., 2008; Figure 6D), which may have aided photosynthetic organisms such as coccolithophores (which produce alkenones). The CO_2 levels dropped slightly during the mid-Holocene (260 ppm), possibly related to regrowth of the terrestrial biosphere. They then rose again in the late Holocene (280 ppm; Luthi et al., 2008) due to rising sea levels and coral reef growth or an increase in Southern Ocean upwelling and a reduction in the efficiency of the biological pump (Studer et al., 2018). There is no evidence from the alkenone concentration (and MAR) data from cores MD97-2121, TAN1106-15, MD97-2120, or TAN1106-43 that these Holocene changes in CO_2 played a strong control in phytoplankton productivity in the SW Pacific, with each core displaying different patterns, during the Holocene (Figure 3a).

We conclude that the primary reason for increased productivity during the early Holocene in the SW Pacific at core site DSDP 594/MD97-2120 (and slightly at MD97-2121) is due to a change in ocean circulation, specifically an expansion of the highly productive STFZ. Previous studies have also suggested a southward expansion, or shift, of the STF during the early Holocene, south of Tasmania (Sikes et al., 2009) and south and east of New Zealand (Bostock et al., 2015; Prebble et al., 2017). The STF is controlled by both bathymetry and winds in this region. The bathymetry has not changed significantly during the Holocene; thus, Prebble et al. (2017) suggest that the expanded STFZ may have been the result of a reduction of the SWW. This has recently been supported by direct wind proxy evidence from a small lake on Macquarie Island immediately

south of New Zealand, which suggested a reduction in SWW during the early Holocene (~54°S; Saunders et al., 2018). Alternatively, there may have been a change in the structure of the SWW (Chiang et al., 2014, 2018). In contrast to other regions of the Southern Hemisphere where the SWW are one jet at ~45°S, in the modern SW Pacific the SWW are split into a subtropical jet (25–30°S) and a subantarctic jet (60°S) during austral winter (Bals-Elsholz et al., 2001; Bostock et al., 2015; Chiang et al., 2014, 2018). Is it possible that the early Holocene saw the initiation of the South Pacific split-jet structure, with an increase in the subtropical jet? The increased subtropical jet may have increased the inflow of STW via the TF to the region, also deepening the winter mixed layer depth, resulting in higher nutrient levels in the early spring at STW core sites H214 and MD97-2121. The enhanced subtropical jet resulted in a weakened subantarctic jet and shifted it south, reducing the winds between 40°S and 55°S over New Zealand and enhancing the jet at the latitude of 55–60°S (Bals-Elsholz et al., 2001; Chiang et al., 2018). This change in the SWW split jet would have also considerably altered the wind stress curl in the SW Pacific, influencing the position and width of the STFZ (and PF) and associated currents such as the SC, within the constraints of the complex bathymetry of the region (Figure 1). Future modeling studies will be needed to test this hypothesis.

5.3. Analog for Productivity Changes in a Warmer World?

The SST and microfossil assemblage results from the transect of cores show that warming during the early Holocene climatic optimum is not spatially uniform across the midlatitudes of the SW Pacific (Prebble et al., 2017). However, these SST spatial variations experienced in the early Holocene closely resemble the future SST pattern from combined ESMs, which show the greatest warming in the STW to the north along the TF, and another patch of greater warming extending over, and south of, Chatham Rise, and less warming in the SAW and little to no warming south of the PF (Law et al., 2017; Rickard et al., 2016). The early Holocene SST changes, however, are significantly lower than those estimated for the end of the century (2100 AD) for RCP8.5 and are closer to those suggested for midcentury (2055 AD) for RCP8.5 or end of the century (2100 AD) for RCP4.5 (Rickard et al., 2016). Thus, the early Holocene climatic optimum may provide an analog for these latter two scenarios.

Under the RCP4.5 2100 and RCP8.5 2055 scenarios, the ESMs predict relatively small declines in the surface nutrients and chlorophyll *a* and a significant small decrease in integrated primary productivity in the STW in the SW Pacific (Rickard et al., 2016). This contrasts with the evidence for a slight increase in "productivity" (from increased CMAR, OMAR, $\delta^{15}N_{bulk}$, and alkenone concentrations) in the STW cores during the early Holocene in this study. To the south, the ESMs display large variations in biogeochemical parameters in the SAW with no significant change (no agreement between models) in surface nutrients (nitrate) and chlorophyll *a* or integrated primary productivity (Law et al., 2017; Rickard et al., 2016).

Notwithstanding the caveats and error ranges of the paleoproductivity proxies and their preservation potential, there are also several reasons why the ESMs from CMIP5 struggle to realistically predict future changes in productivity in the SW Pacific. First, several of the ESMs in CMIP5 do not have realistic SWW for this region (i.e., no split-jet structure for the SW Pacific; Chiang et al., 2018). Using only ESMs with a split-jet structure (e.g., HadGEM), downscaled, high-resolution climate models for the SW Pacific suggest a shift to a more dominant subtropical jet under future climate change (S. Dean, personal communication, October 2018), a situation similar to the conditions proposed here for the early Holocene. The split-jet structure alters the wind stress curl in the region and thus affects the local oceanographic circulation (Chiang et al., 2018). Second, the low resolution of the ESMs (in the order of 1° to 3.75°) does not allow them to resolve boundary currents or oceanic eddy activity. In contrast to these low-resolution CMIP5 results, a high-resolution ocean eddy-resolving model (0.1°) of the Tasman Sea, west of New Zealand, suggests an increase in eddy activity, which results in greater nutrient supply to the upper oligotrophic surface waters and increased productivity under future climate change in the STW (Matear et al., 2013). Thus, significant improvements are needed in the atmospheric forcing, resolution, and the biogeochemistry parameterization in the ESMs in order to realistically forecast the future ocean productivity of the oceanographically complex SW Pacific.

We also recommend that future paleoceanographic work should focus on other warmer interglacials (Marine Isotope Stage 5e or Marine Isotope State 11), which may provide better analogs for climate change by the end of the century under the more extreme RCP8.5 scenario. These future studies should also include a wider range of environmental (e.g., stratification/mixing) and productivity proxies (e.g., coccolithophore assemblages), as well as flux measurements.

6. Conclusions

We used a range of proxies to assess changes in productivity along a latitudinal (36–58°S) transect of marine sediment cores in the SW Pacific. During the early Holocene there is a slight increase in productivity at the STW core sites (H214; MD97-2121), no increase in the STFZ core site (TAN1106-15), and an increase in one of the core sites (DSDP 594/MD97-2120) immediately south of the STF, but not the other (TAN1106-43). The data from the core close to the PF (TAN1302–96) show an increase during the mid-Holocene rather than during the early Holocene. The increase in productivity at the DSDP 594/MD97-2120 core site is accompanied by higher SST (2–3 °C) and is interpreted as an expansion of the STFZ over this site. There is no statistically significant increase in SST (within the error ± 1 °C) at other core sites, but changes in the foraminiferal and dinoflagellate assemblages suggest that there were changes in the ocean circulation of the SW Pacific at this time that subtly influenced the productivity. These changes in ocean circulation were most likely driven by changes in the SWW with the strengthening of the split-jet structure in this region and the dominance of the subtropical jet over the subantarctic jet, altering the regional wind stress curl and influencing the position of the ocean fronts, within the constraints of the local bathymetry. The limited warming at most of the core sites during the early Holocene suggests that this time period may provide a suitable analog for ocean productivity under future climate change for the midcentury (2055) under RCP8.5 or end of century (2100) under RCP4.5 and that high-resolution models with realistic winds and improved biogeochemistry models will be required to realistically predict future changes in this oceanographically complex region. Future work should also focus on warmer interglacials such as MIS5e and MIS11 as better analogues for a warmer world at the end of the century (RCP 8.5; 2100 AD).

Acknowledgments
This project was funded by the New Zealand Antarctic Research Institute (NZARI), with cofunding from NIWA core funding Coasts and Oceans Physical Resources program and GNS Global Change through Time program. This research was supported by KOPRI project (PE18030). We would like to thank Graham Rickard, Sara Mikaloff-Fletcher, and Erik Behrens for their insights into the CMIP5 models and two anonymous reviewers. This work is a contribution to INQUA PALCOMM project 1302 SHAPE: Southern Hemisphere Assessment of Palaeo-Environments. The data from this paper will be available at the Pangaea.de database.

References

Altabet, M. A., & Francois, R. (1994). Sedimentary nitrogen isotopic ratio as a recorder for surface ocean nitrate utilization. *Global Biogeochemical Cycles*, *8*(1), 103–116. https://doi.org/10.1029/93GB03396

Anderson, R. F., Ali, S., Bradtmiller, L. I., Nielsen, S. H. H., Fleisher, M. Q., Anderson, B. E., & Burckle, L. H. (2009). Wind-driven upwelling in the Southern Ocean and the deglacial rise in atmospheric CO_2. *Science*, *323*(5920), 1443–1448. https://doi.org/10.1126/science.1167441

Bals-Elsholz, T. M., Atallah, E. H., Bosart, L. F., Wasula, T. A., Cempa, M. J., & Lupo, A. R. (2001). The wintertime Southern Hemisphere split jet: Structure, variability and evolution. *Journal of Climate*, *14*(21), 4191–4215. https://doi.org/10.1175/1520-0442(2001)014<4191:TWSHSJ>2.0.CO;2

Barrows, T. T., Juggins, S., De Deckker, P., Calvo, E., & Pelejero, C. (2007). Long term sea surface temperature and climate change in the Australian-New Zealand region. *Paleoceanography*, *22*, PA2215. https://doi.org/10.1029/2006PA001328

Belkin, I. M., & Gordon, A. L. (1996). Southern Ocean fronts from the Greenwich meridian to Tasmania. *Journal of Geophysical Research*, *101*(C2), 3675–3696. https://doi.org/10.1029/95JC02750

Bostock, H. C., Barrows, T. T., Carter, L., Chase, Z., Cortese, G., Dunbar, G. B., et al. (2013). A review of the Australian-New Zealand sector of the Southern Ocean over the last 30 ka (Aus-INTIMATE project). *Quaternary Science Reviews*, *74*, 35–57. https://doi.org/10.1016/j.quascirev.2012.07.018

Bostock, H. C., Hayward, B. W., Neil, H. L., Currie, K. I., & Dunbar, G. B. (2011). Deep-water carbonate concentrations in the southwest Pacific. *Deep Sea Research Part I: Oceanographic Research Papers*, *58*(1), 72–85. https://doi.org/10.1016/j.dsr.2010.11.010

Bostock, H. C., Hayward, B. W., Neil, H. L., Sabaa, A. T., & Scott, G. H. (2015). Changes in the position of the Subtropical Front south of New Zealand since the last glacial period. *Paleoceanography*, *30*, 824–844. https://doi.org/10.1002/2014PA002652

Bostock, H. C., Opdyke, B. N., Gagan, M. K., Kiss, A. E., & Fifield, L. K. (2006). Glacial/interglacial changes in the East Australian Current. *Climate Dynamics*, *26*(6), 645–659. https://doi.org/10.1007/s00382-005-0103-7

Boyd, P., LaRoche, J., Gall, M., Frew, R., & McKay, R. M. L. (1999). Role of iron, light, and silicate in controlling algal biomass in subantarctic waters SE of New Zealand. *Journal of Geophysical Research*, *104*, 13,391–13,404.

Boyd, P. W., McTainsh, G., Sherlock, V., Richardson, K., Nichol, S., Ellwood, M., & Frew, R. (2004). Episodic enhancement of phytoplankton stocks in New Zealand subantarctic waters: Contribution of atmospheric and oceanic iron supply. *Global Biogeochemical Cycles*, *18*, GB1029. https://doi.org/10.1029/2002GB002020

Boyd, P. W., Watson, A. J., Law, C. S., Abraham, E. R., Trull, T., Murdoch, R., et al. (2000). A mesoscale phytoplankton bloom in the polar Southern Ocean stimulated by iron fertilization. *Nature*, *407*(6805), 695–702. https://doi.org/10.1038/35037500

Bradtmiller, L. I., Anderson, R. F., Fleisher, M. Q., & Burckle, L. H. (2009). Comparing glacial and Holocene opal fluxes in the Pacific sector of the Southern Ocean. *Paleoceanography*, *24*, PA2214. https://doi.org/10.1029/2008PA001693

Broecker, W. S. (1982a). Glacial to interglacial changes in ocean chemistry. *Progress in Oceanography*, *11*(2), 151–197. https://doi.org/10.1016/0079-6611(82)90007-6

Broecker, W. S. (1982b). Ocean chemistry during glacial time. *Geochimica et Cosmochimica Acta*, *46*(10), 1689–1705. https://doi.org/10.1016/0016-7037(82)90110-7

Butzin, M., Prange, M., & Lohmann, G. (2005). Radiocarbon simulations for the glacial ocean: The effects of wind stress, Southern Ocean sea ice and Heinrich events. *Earth and Planetary Science Letters*, *235*(1-2), 45–61. https://doi.org/10.1016/j.epsl.2005.03.003

Calvo, E., Pelejero, C., & Logan, G. A. (2003). Pressurized liquid extraction of selected molecular biomarkers in deep sea sediments used as proxies in paleoceanography. *Journal of Chromatography A*, *989*(2), 197–205. https://doi.org/10.1016/S0021-9673(03)00119-5

Calvo, E., Pelejero, C., Logan, G. A., & De Deckker, P. (2004). Dust-induced changes in phytoplankton composition in the Tasman Sea during the last four glacial cycles. *Paleoceanography*, *19*, PA2020. https://doi.org/10.1029/2003PA000992

Carter, L., & Manighetti, B. (2006). Glacial/interglacial control of terrigenous and biogenic fluxes in the deep ocean off a high input, collisional margin: A 139 kyr record from New Zealand. *Marine Geology*, *226*(3-4), 307–322. https://doi.org/10.1016/j.margeo.2005.11.004

Carter, L., Manighetti, B., Ganssen, G., & Northcote, L. (2008). Southwest Pacific modulation of abrupt climate change during the Antarctic Cold Reversal–Younger Dryas. *Palaeogeography Palaeoclimatology Palaeoecology*, *260*(1-2), 284–298. https://doi.org/10.1016/j.palaeo.2007.08.013

Carter, L., Neil, H. L., & McCave, I. N. (2000). Glacial to interglacial changes in non-carbonate and carbonate accumulation in the SW Pacific Ocean, New Zealand. *Palaeogeography, Palaeoclimatology, Palaeoecology*, *162*(3-4), 333–356. https://doi.org/10.1016/S0031-0182(00)00137-1

Chase, Z., Anderson, R. F., Fleisher, M. Q., & Kubik, P. W. (2003). Accumulation of biogenic and lithogenic material in the Pacific sector of the Southern Ocean during the past 40,000 years. *Deep-Sea Research Part II*, *50*(3-4), 799–832. https://doi.org/10.1016/S0967-0645(02)00595-7

Chiang, J. C. H., Lee, S.-Y., Putnam, A. E., & Wang, X. (2014). South Pacific Split jet, ITCZ shifts, and atmospheric north–south linkages during abrupt climate changes of the last glacial period. *Earth and Planetary Science Letters*, *406*, 233–246. https://doi.org/10.1016/j.epsl.2014.09.012

Chiang, J. C. H., Tokos, K. S., Lee, S.-Y., & Matsumoto, K. (2018). Contrasting impacts of the South Pacific Split Jet and the Southern Annular Mode modulation on Southern Ocean circulation and biogeochemistry. *Paleoceanography and Paleoclimatology*, *33*, 2–20. https://doi.org/10.1002/2017PA003229

Chiswell, S. M., Bostock, H. C., Sutton, P. J. H., & Williams, M. J. M. (2015). Physical oceanography of the deep seas around New Zealand: A review. *New Zealand Journal of Marine and Freshwater Research*, *49*(2), 286–317. https://doi.org/10.1080/00288330.2014.992918

Chiswell, S. M., Bradford-Grieve, J., Hadfield, M. G., & Kennan, S. C. (2013). Climatology of surface chlorophyll a, autumn-winter and spring blooms in the Southwest Pacific Ocean. *Journal of Geophysical Research: Oceans*, *118*, 1003–1018. https://doi.org/10.1002/jgrc.20088

Crundwell, M., Scott, G., Naish, T., & Carter, L. (2008). Glacial–interglacial ocean climate variability from planktonic foraminifera during the mid-Pleistocene transition in the temperate southwest Pacific, ODP site 1123. *Palaeogeography Palaeoclimatology Palaeoecology*, *260*(1-2), 202–229. https://doi.org/10.1016/j.palaeo.2007.08.023

Duggen, S., Olgun, N., Croot, P., Hoffmann, L. J., Dietze, H., Delmelle, P., & Teschner, C. (2010). The role of airborne volcanic ash for the surface ocean biogeochemical iron-cycle: A review. *Biogeosciences*, *7*(3), 827–844. https://doi.org/10.5194/bg-7-827-2010

Durand, A., Chase, Z., Noble, T. L., Bostock, H., Jaccard, S. L., Kitchener, P., et al. (2017). Export production in the New-Zealand region since the Last Glacial Maximum. *Earth and Planetary Science Letters*, *469*, 110–122.

Ellis, D. B., & Moore, T. C. Jr. (1973). Calcium carbonate, opal, and quartz in Holocene pelagic sediments and the calcite compensation level in the South Atlantic Ocean. *Journal of Marine Research*, *31*(3), 210–227.

Ellwood, M. J., Boyd, P. W., & Sutton, P. (2008). Winter-time dissolved iron and nutrient distributions in the subantarctic zone from 40–52S; 155–160E. *Geophysical Research Letters*, *35*, L11604. https://doi.org/10.1029/2008GL033699

Ellwood, M. J., Law, C. S., Hall, J., Woodward, E. M. S., Strzepek, R., Kuparinen, J., et al. (2013). Relationships between nutrient stocks and inventories and phytoplankton physiological status along an oligotrophic meridional transect in the Tasman Sea. *Deep Sea Research Part I: Oceanographic Research Papers*, *72*, 102–120. https://doi.org/10.1016/j.dsrx.2012.11.001

Franck, V. M., Bruland, K. W., Hutchins, D. A., & Brzezinski, M. A. (2003). Iron and zinc effects on silicic acid and nitrate uptake kinetics in three high-nutrient, low-chlorophyll (HNLC) regions. *Marine Ecology Progress Series*, *252*, 15–33. https://doi.org/10.3354/meps252015

Francois, R., Altabet, M. A., Yu, E.-F., Sigman, D. M., Bacon, M. P., Frank, M., et al. (1997). Contribution of Southern Ocean surface-water stratification to low atmospheric CO_2 concentrations during the last glacial period. *Nature*, *389*, 929–935.

Galbraith, E., Kienast, M., & NICOPP Working Group (2013). The acceleration of oceanic denitrification during deglacial warming. *Nature Geoscience*, *6*(7), 579–584. https://doi.org/10.1038/ngeo1832

Graham, R. M., De Boer, A. M., van Sebille, E., Kohfeld, K. E., & Schlosser, C. (2015). Inferring source regions and supply mechanisms of iron in the Southern Ocean from satellite chlorophyll data. *Deep Sea Research Part I: Oceanographic Research Papers*, *104*, 9–25. https://doi.org/10.1016/j.dsr.2015.05.007

Haslett, J., & Parnell, A. (2008). A simple monotone process with application to radiocarbon-dated depth chronologies. *Journal of the Royal Statistical Society. Series C: Applied Statistics*, *57*(4), 399–418. https://doi.org/10.1111/j.1467-9876.2008.00623.x

Jones, G. A., & Kaiteris, P. (1983). A vacuum gasometric technique for rapid and precise analysis of calcium carbonate in sediments and soils. *Journal of Sedimentary Petrology*, *53*(2), 655–660. https://doi.org/10.1306/212F825B-2B24-11D7-8648000102C1865D

Kienast, M., Higginson, M. J., Mollenhauer, G., Eglinton, T. I., Chen, M.-T., & Calvert, S. E. (2005). On the sedimentological origin of down-core variations of bulk sedimentary nitrogen isotope ratios. *Paleoceanography*, *20*, PA2009. https://doi.org/10.1029/2004PA001081

King, A. L., & Howard, W. R. (2001). Seasonality of foraminiferal flux in sediment traps at Chatham Rise, SW Pacific: Implications for paleotemperature estimates. *Deep Sea Research Part I: Oceanographic Research Papers*, *48*(7), 1687–1708. https://doi.org/10.1016/S0967-0637(00)00106-0

Kowalski, E. A., & Meyers, P. A. (1997). Glacial-interglacial variations in Quaternary production of marine organic matter at DSDP site 594, Chatham Rise, southeastern New Zealand margin. *Marine Geology*, *140*(3-4), 249–263. https://doi.org/10.1016/S0025-3227(97)00044-3

Lambert, F., Bigler, M., Steffensen, J. P., Hutterli, M., & Fisher, H. (2012). Centennial mineral dust variability in high-resolution ice core data from Dome C, Antarctica. *Climate of the Past*, *8*(2), 609–623. https://doi.org/10.5194/cp-8-609-2012

Law, C. S., Rickard, G. J., Mikaloff-Fletcher, S. E., Pinkerton, M. H., Behrens, E., Chiswell, S. M., & Currie, K. (2017). Climate change projections for the surface ocean around New Zealand. *New Zealand Journal of Marine and Freshwater Research*, *52*(3), 309–335. https://doi.org/10.1080/00288330.2017.1390772

Law, C. S., Woodward, E. M. S., Ellwood, M. J., Marriner, A., Bury, S. J., & Safi, K. A. (2011). Response of surface nutrient inventories and nitrogen fixation to a tropical cyclone in the southwest Pacific. *Limnology and Oceanography*, *56*(4), 1372–1385. https://doi.org/10.4319/lo.2011.56.4.1372

Lowe, D. J., Blaauw, M., Hogg, A. G., & Newnham, R. M. (2013). Ages of 24 widespread tephras erupted since 30,000 years ago in New Zealand, with re-evaluation of the timing and palaeoclimatic implications of the Lateglacial cool episode recorded at Kaipo bog. *Quaternary Science Reviews*, *74*, 170–194. https://doi.org/10.1016/j.quascirev.2012.11.022

Lüthi, D., le Floch, M., Bereiter, B., Blunier, T., Barnola, J.-C., Siegenthaler, U., et al. (2008). High-resolution carbon dioxide concentration record 650,000–800,000 years before present. *Nature*, *453*(7193), 379–382. https://doi.org/10.1038/nature06949

Marcott, S. A., Shakun, J. D., Clark, P. U., & Mix, A. C. (2013). A reconstruction of regional and global temperature for the past 11,300 years. *Science*, *339*(6124), 1198–1201. https://doi.org/10.1126/science.1228026

Marr, J. P., Carter, L., Bostock, H. C., Bolton, A., & Smith, E. (2013). Southwest Pacific Ocean response to a warming world: Using Mg/Ca, Zn/Ca, and Mn/Ca in foraminifera to track surface ocean water masses during the last deglaciation. *Paleoceanography*, *28*, 347–362. https://doi.org/10.1002/palo.20032

Matear, R. J., Chamberlain, M. A., Sun, C., & Feng, M. (2013). Climate change projection of the Tasman Sea from an eddy-resolving ocean model. *Journal of Geophysical Research: Oceans*, *118*, 2961–2976. https://doi.org/10.1002/jgrc.20202

Mortlock, R. A., & Froelich, P. N. (1989). A simple method for the rapid determination of biogenic opal in pelagic marine sediments. *Deep Sea Research Part A: Oceanographic Research Papers*, *36*(9), 1415–1426. https://doi.org/10.1016/0198-0149(89)90092-7

Murphy, R. J., Pinkerton, M. H., Richardson, K. M., Bradford-Grieve, J. M., & Boyd, P. W. (2001). Phytoplankton distributions around New Zealand derived from SeaWiFS remotely sensed ocean colour data. *New Zealand Journal of Marine and Freshwater Research*, *35*(2), 343–362. https://doi.org/10.1080/00288330.2001.9517005

Neil, H. L., Carter, L., & Morris, M. Y. (2004). Thermal isolation of Campbell Plateau, New Zealand, by the Antarctic Circumpolar Current over the past 130 kyr. *Paleoceanography*, *19*, PA4008. https://doi.org/10.1029/2003PA000975

Nelson, C. S., Cooke, P. J., Hendy, C. H., & Cuthbertson, A. M. (1993). Oceanographic and climatic changes over the past 160,000 years at Deep Sea Drilling Project site 594 off southeastern New Zealand, Southwest Pacific Ocean. *Paleoceanography*, *8*(4), 435–458. https://doi.org/10.1029/93PA01162

Nodder, S. D., Boyd, P. W., Chiswell, S. M., Pinkerton, M. H., Bradford-Grieve, J. M., & Greig, M. J. N. (2005). Temporal coupling between surface and deep ocean biogeochemical processes in contrasting subtropical and subantarctic water masses, southwest Pacific Ocean. *Journal of Geophysical Research*, *110*, C12017. https://doi.org/10.1029/2004JC002833

Nodder, S. D., Chiswell, S. M., & Northcote, L. C. (2016). Annual cycles of deep-ocean biogeochemical export fluxes in subtropical and subantarctic waters, southwest Pacific Ocean. *Journal of Geophysical Research: Oceans*, *121*, 2405–2424. https://doi.org/10.1002/2015JC011243

Nodder, S. D., & Northcote, L. C. (2001). Episodic particulate fuxes at southern temperate mid-latitudes (42-45°S) in the Subtropical Front region, east of New Zealand. *Deep-Sea Research Part I*, *48*(3), 833–864. https://doi.org/10.1016/S0967-0637(00)00062-5

Orsi, A. H., Whitworth, T., & Nowlin, W. D. (1995). On the meridional extent and fronts of the Antarctic Circumpolar Current. *Deep-Sea Research Part I*, *42*(5), 641–673. https://doi.org/10.1016/0967-0637(95)00021-W

Pahnke, K., & Sachs, J. P. (2006). Sea surface temperatures of southern midlatitudes 0–160 kyr B.P. *Paleoceanography*, *21*, PA2003. https://doi.org/10.1029/2005PA001191

Pahnke, K., Zahn, R., Elderfield, H., & Schulz, M. (2003). 340,000-year centennial-scale marine record of southern hemisphere climatic oscillation. *Science*, *301*, 948–952.

Prebble, J. G., Bostock, H. C., Cortese, G., Lorrey, A. M., Hayward, B. W., Calvo, E. C., et al. (2017). Evidence for a Holocene climatic optimum in the southwest Pacific: A multiproxy study. *Paleoceanography*, *32*, 763–779. https://doi.org/10.1002/2016PA003065

Prebble, J. G., Crouch, E. M., Carter, L., Cortese, G., Bostock, H., & Neil, H. (2013). An expanded modern dinoflagellate cyst dataset for the Southwest Pacific and Southern Hemisphere with environmental associations. *Marine Micropaleontology*, *101*, 33–48. https://doi.org/10.1016/j.marmicro.2013.04.004

Prebble, J. G., Crouch, E. M., Carter, L., Cortese, G., & Nodder, S. D. (2013). Dinoflagellate cysts from two sediment traps east of New Zealand. *Marine Micropaleontology*, *104*, 25–37. https://doi.org/10.1016/j.marmicro.2013.08.003

Reimer, P. J., Bard, E., Bayliss, A., Beck, J. W., Blackwell, P. G., Ramsey, C. B., et al. (2013). IntCal13 and Marine13 radiocarbon age calibration curves 0–50,000 years cal BP. *Radiocarbon*, *55*(04), 1869–1887. https://doi.org/10.2458/azu_js_rc.55.16947

Richter, T. O., Van der Gaast, S., Koster, B., Vaars, A., Gieles, R., de Stigter, H. C., de Haas, H., & van Weering, T. C. E. (2006). The Avaatech XRF Core Scanner: technical description and applications to NE Atlantic sediments. In R. G. Rothwell (Ed.), *New techniques in sediment core analysis*. *Geological Society, London, Special Publications, 267*, 39–50. https://doi.org/10.1144/GSL.SP.2006.267.01.03

Rickard, G., Behrens, E., & Chiswell, S. M. (2016). CMIP5 earth system models with biogeochemistry: An assessment for the southwest Pacific Ocean. *Journal of Geophysical Research: Oceans*, *121*, 7857–7879. https://doi.org/10.1002/2016JC011736

Robinson, R. S., Kienast, M., Albuquerque, A. L., Altabet, M., Contreras, S., De Pol Hoz, R., et al. (2012). A review of nitrogen isotopic alteration in marine sediments. *Paleoceanography*, *27*, PA4203. https://doi.org/10.1029/2012PA002321

Robinson, R. S., & Sigman, D. M. (2008). Nitrogen isotopic evidence for a poleward decrease in surface nitrate within the ice age Antarctic. *Quaternary Science Reviews*, *27*(9-10), 1076–1090. https://doi.org/10.1016/j.quascirev.2008.02.005

Rothwell, R. G., & Croudace, I. W. (2015). Twenty years of XRF core scanning marine sediments: What do geochemical proxies tell us? In I. W. Croudace, & R. G. Rothwell (Eds.), Developments in Paleoenvironmental Research 17*Micro-XRF studies of sediment cores: Applications of a non-destructive tool for the environmental sciences* (Chapter 2, pp. 25–102). Springer.

Sachs, J. P., & Anderson, R. F. (2005). Increased productivity in the subantarctic ocean during Heinrich events. *Nature*, *434*(7037), 1118–1121. https://doi.org/10.1038/nature03544

Samson, C. R., Sikes, E. L., & Howard, W. R. (2005). Deglacial paleoceanographic history of the Bay of Plenty, New Zealand. *Paleoceanography*, *20*, PA4017. https://doi.org/10.1029/2004PA001088

Saunders, K. M., Roberts, S. J., Perren, B., Butz, C., Sime, L., Davies, S., et al. (2018). Holocene dynamics of the Southern Hemisphere Westerly Winds and possible links to CO_2 outgassing. *Nature Geoscience*, *11*(9), 650–655. https://doi.org/10.1038/s41561-018-0186-5

Scott, G. H. (2013). Planktonic foraminifera as oceanographic proxies: Comparison of biogeographic classifications using some southwest Pacific core-top faunas. *ISRN Oceanography*, *2013*, 1–15. https://doi.org/10.5402/2013/508184

Sikes, E. L., Howard, W. R., Samson, C. R., Mahan, T. S., Robertson, L. G., & Volkman, J. K. (2009). Southern Ocean seasonal temperature and Subtropical Front movement on the South Tasman Rise in the late Quaternary. *Paleoceanography*, *24*, PA2201. https://doi.org/10.1029/2008PA001659

Sikes, E. L., O'Leary, T., Nodder, S. D., & Volkman, J. K. (2005). Alkenone temperature records and biomarker flux at the Subtropical Front on the Chatham Rise, SW Pacific Ocean. *Deep Sea Research Part I: Oceanographic Research Papers*, *52*(5), 721–748. https://doi.org/10.1016/j.dsr.2004.12.003

Smith, R. O., Vennell, R., Bostock, H. C., & Williams, M. J. M. (2013). Interaction of the Subtropical Front with topography around southern New Zealand. *Deep-Sea Research Part I*, *76*, 13–26. https://doi.org/10.1016/j.dsr.2013.02.007

Sokolov, S., & Rintoul, S. R. (2009). Circumpolar structure and distribution of the Antarctic Circumpolar Current fronts: 1. Mean circumpolar paths. *Journal of Geophysical Research*, *114*, C11018. https://doi.org/10.1029/2008JC005108

Sokolov, S., Rintoul, S. R., & Wienecke, B. (2006). Tracking the Polar Front south of New Zealand using penguin dive data. *Deep-Sea Research Part I*, *53*(4), 591–607. https://doi.org/10.1016/j.dsr.2005.12.012

Studer, A. S., Sigman, D. M., Martinez-Garcia, A., Thole, L. M., Michel, E., Jaccard, S. L., et al. (2018). Increased nutrient supply to the Southern Ocean during the Holocene and its implications for the pre-industrial atmospheric CO_2 rise. *Nature Geoscience*, *11*(10), 756–760. https://doi.org/10.1038/s41561-018-0191-8

Sutton, P. J. H. (2003). The Southland Current: A subantarctic current. *New Zealand Journal of Marine and Freshwater Research*, *37*(3), 645–652. https://doi.org/10.1080/00288330.2003.9517195

Uddstrom, M. J., & Oien, N. A. (1999). On the use of high-resolution satellite data to describe the spatial and temporal variability of sea surface temperatures in the New Zealand region. *Journal of Geophysical Research*, *104*(C9), 20,729–20,751. https://doi.org/10.1029/1999JC900167

Walker, M. J. C., Berkelhammer, M., Björck, S., Cwynar, L. C., Fisher, D. A., Long, A. J., et al. (2012). Formal subdivision of the Holocene Series/Epoch: A discussion paper by a working group of INTIMATE (Integration of ice-core, marine and terrestrial records) and the Subcommission on Quaternary Stratigraphy (International Commission on Stratigraphy). *Journal of Quaternary Science*, *27*(7), 649–659. https://doi.org/10.1002/jqs.2565

Wells, P., & Okada, H. (1997). Response of nannoplankton to major changes in sea-surface temperature and movements of hydrological fronts over Site DSDP 594 (south Chatham Rise, southeastern New Zealand), during the last 130 kyr. *Marine Micropaleontology*, *32*, 341–363.

Zonneveld, K. A. F., Versteegh, G., & Kodrans-Nsiah, M. (2008). Preservation and organic chemistry of late Cenozoic organic-walled dinoflagellate cysts: A review. *Marine Micropaleontology*, *68*(1-2), 179–197. https://doi.org/10.1016/j.marmicro.2008.01.015

Zonneveld, K. A. F., Versteegh, G. J. M., & de Lange, G. J. (1997). Preservation of organic-walled dinoflagellate cysts in different oxygen regimes: A 10,000 year natural experiment. *Marine Micropaleontology*, *29*(3-4), 393–405. https://doi.org/10.1016/S0377-8398(96)00032-1

Zonneveld, K. A. F., Versteegh, G. J. M., Kasten, S., Eglinton, T. I., Emeis, K. C., Huguet, C., et al. (2010). Selective preservation of organic matter in marine environments; processes and impact on the sedimentary record. *Biogeosciences*, *7*(2), 483–511. https://doi.org/10.5194/bg-7-483-2010